

# Observation of the Higgs boson decaying to photons with the CMS detector using p-p collisions at 13 TeV

Louie Dartmoor Corpe  
of Imperial College London

A dissertation submitted to Imperial College London  
for the degree of Doctor of Philosophy

The copyright of this thesis rests with the author and is made available under a Creative Commons Attribution Non-Commercial No Derivatives licence. Researchers are free to copy, distribute or transmit the thesis on the condition that they attribute it, that they do not use it for commercial purposes and that they do not alter, transform or build upon it. For any reuse or redistribution, researchers must make clear to others the licence terms of this work.

# Abstract

lorem ispum

## Declaration

Louie Dartmoor Corpe

## Acknowledgements

# Contents

<b>List of figures</b>	<b>vii</b>
<b>List of tables</b>	<b>1</b>
<b>1 Introduction and theory</b>	<b>1</b>
<b>2 Overview of the LHC and CMS</b>	<b>2</b>
2.1 The Large Hadron Collider (LHC) . . . . .	2
2.2 The Compact Muon Solenoid (CMS) . . . . .	5
2.2.1 Overview . . . . .	5
2.2.2 Tracker . . . . .	6
2.2.3 Electromagnetic Calorimeter (ECAL) . . . . .	8
2.2.4 Hadronic Calorimeter (HCAL) . . . . .	12
2.2.5 Muon detectors . . . . .	14
2.2.6 Trigger and data processing . . . . .	16
<b>Bibliography</b>	<b>19</b>
<b>Acronyms</b>	<b>21</b>

# List of figures

2.1	Schematic view of the CERN accelerator complex, showing the chain of machines which allow particles to be accelerated to 6.5 TeV: LINAC2, PS Booster, PS, SPS and finally LHC.[8] . . . . .	4
2.2	Overview of the integrated luminosity delivered by the LHC throughout its operation until the time of writing, as recorded by CMS.[9] . . . . .	5
2.3	A cutaway diagram of the CMS detector, showing the main components and subdetectors, which are described in Section 2.4[10]. . . . .	6
2.4	A diagram showing the layout of the CMS tracker components: the pixel tracker (labelled PIXEL) is the nearest to the interaction region marked by the black dot. The various sections of the strip tracker (TIB, TID, TOB, TEC+ and TEC-) are arranged around the pixel tracker[10] . . . .	7
2.5	Schematic cross section of one quadrant of the ECAL, showing the arrangement of crystals in the ECAL barrel (EB) and endcaps (EE)[13]. The shower detector (SE, referred to as ES in the text) is also visible, as is the hadron calorimeter barrel (HB) and the tracker (TK). . . . .	9
2.6	The response of the CMS ECAL lead tungstate crystals is shown as a function of time, and for different pseudorapidity ranges. The crystal response worsens as data are collected, due to transparency loss caused by exposure to radiation. During shutdown periods, the response recovers somewhat thanks to spontaneous annealing[16] . . . . .	12
2.7	The normalised value of the invariant mass of the $\pi^0$ particle in its decay to photons, as measured by the CMS ECAL barrel, with and without the Laser Monitoring (LM) corrections for crystal transparency loss, showing the degradation of the response of the lead tungstate crystals, even over a period of hours[16] . . . . .	13

- 
- 2.8 Schematic cross section of one quadrant of the HCAL, showing the arrangement of the various components of the sub-detector: The HB and HE surrounding the ECAL, with the HF at high  $\eta$  and the HO just outside of the solenoid[5]. . . . . 14
- 2.9 Schematic cross section of one quadrant of the CMS muon detector, showing the arrangement of the various components of the sub-detector: The DTs in the barrel, and CSCs in the endcaps and the RPCs in both[19]. 15



## List of tables

# Chapter 1

## Introduction and theory

# Chapter 2

## Overview of the LHC and CMS

### 2.1 The Large Hadron Collider (LHC)

The Large Hadron Collider (LHC) [1] is a synchrotron of diameter 27 km, currently the largest and most powerful in the world, that was installed in the tunnel which previously contained the Large Electron-Positron Collider (LEP) [2] collider at the European Organization for Nuclear Research (CERN). The tunnel is located roughly 100 m underground near Geneva, on the border between Switzerland and France. The LHC was designed to perform collisions of two types: p-p (proton-proton) collisions and, less frequently, heavy ion collisions, for example Pb-Pb (lead-lead). The former is used to search for new particles and perform standard model (SM) measurements, such as the ones presented in this thesis. The latter is used, for example, for studies of quark-gluon plasma, and is not discussed in detail here.

The LHC is the last stage in a series of accelerators which form the CERN accelerator complex, which is illustrated in Figure 2.1. The procedure by which particles are accelerated using this chain of machines is described in [1], and is summarised below. In p-p collisions, protons are first obtained from a hydrogen gas, which is stripped of electrons. The particles are then brought up to an energy of 50 MeV using Linear Accelerator 2 (LINAC2). The particles coming out of the initial linear accelerator are transferred into the Proton Synchrotron Booster (PSB), which raises the beam energy to 1.4 GeV, before the beams enter the Proton Synchrotron (PS). At this stage, the protons are accelerated to 25 GeV. Once the beams reach the required energy, they are passed into the Super Proton Synchrotron (SPS), and accelerated to 450 GeV, before finally being injected into the LHC ring. The LHC then brings the beams up to their final energy, which, in the most recent run, was approximately 6.5 TeV, leading to a combined

centre-of-mass (CoM) energy of 13 TeV when the beams are focussed and made to collide at the four interaction points along the ring. A further increase in the beam energy is foreseen in the LHC programme, which would bring it up to its design value of 7 TeV per beam, and CoM energy of 14 TeV.

The counter-circling beams in the LHC are bunched such that they will collide at specific intervals of time, with each bunch containing several billion protons. This bunch spacing was 50 ns in the initial running of the LHC, but has now been dropped to its design value of 25 ns, to allow a faster accumulation of data. The number of times a process occurs per second in collision experiments ( $N_{\text{process}}$ ) can be obtained from the following relation [3]:

$$N_{\text{process}} = \sigma_{\text{process}} \times L, \quad (2.1)$$

where  $\sigma_{\text{process}}$  is the cross-section of the considered process and  $L$  is the instantaneous luminosity.  $L$  depends only on the machine parameters, and assuming a Gaussian beam distribution, is given by the relation [3]:

$$L = \frac{n_b N_b^2 f_{\text{rev}} \gamma_r}{4\pi \epsilon_n \beta^*} F, \quad (2.2)$$

where  $n_b$  is the number of bunches in each beam,  $N_b$  is the number of particles per bunch,  $f_{\text{rev}}$  is the revolution frequency,  $\gamma_r$  is the relativistic gamma factor,  $\epsilon_n$  is the normalised transverse beam emittance,  $\beta^*$  is the beta function at the collision point and  $F$  is a luminosity reduction factor which takes into account the fact that beams cross at a slight angle. Each instance where the data from a bunch crossing are saved by the detector is known as an event. Typically, an event will have a single interaction which is of interest. At 13 TeV the p-p interaction cross-section is very large, so several interactions per crossing are expected. The physical locations of these interactions are referred to as vertices, with the interaction of interest occurring at the primary vertex (PV), and other interactions at secondary vertices. The additional interactions in an event, other than the one occurring at the PV, are collectively referred to as pile-up (PU).

The LHC began operation in 2010 at a CoM energy of 7 TeV, collecting  $44 \text{ pb}^{-1}$  in 2010 and  $6.1 \text{ fb}^{-1}$  in 2011. In 2012, the CoM energy was successfully increased to 8 TeV and  $23.3 \text{ fb}^{-1}$  were recorded. This period corresponded to the first physics run of the LHC (Run I). After a shutdown period for planned upgrades to the machine, the LHC began

Run II and raised its CoM energy to 13 TeV, delivering  $4.3 \text{ fb}^{-1}$  in 2015 and  $32.4 \text{ fb}^{-1}$  in 2016, as can be seen in Figure 2.2. The instantaneous luminosity of the LHC is currently at its design value of  $10^{34} \text{ cm}^{-2} \text{ s}^{-1}$ . Run II is scheduled to continue until 2018 before another shutdown for upgrades is envisaged.

The LHC beams are focused and crossed, to collide at four different points along the ring, where the ATLAS [4], Compact Muon Solenoid (CMS) [5], ALICE [6] and LHCb [7] experiments collect the resulting data. This thesis deals with results collected using the CMS detector, which is described in detail below.

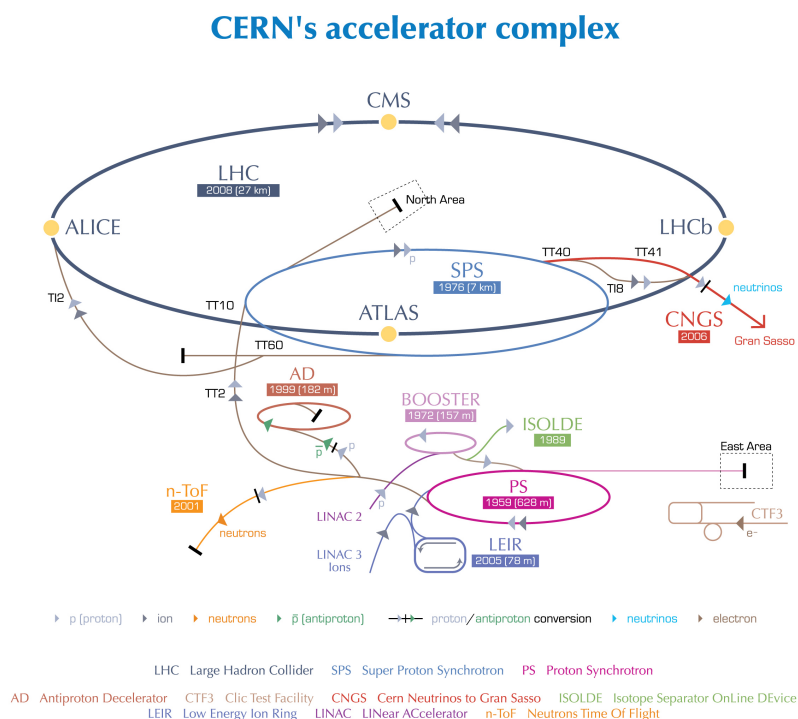


**Figure 2.1:** Schematic view of the CERN accelerator complex, showing the chain of machines which allow particles to be accelerated to 6.5 TeV: LINAC2, PS Booster, PS, SPS and finally LHC. [8]

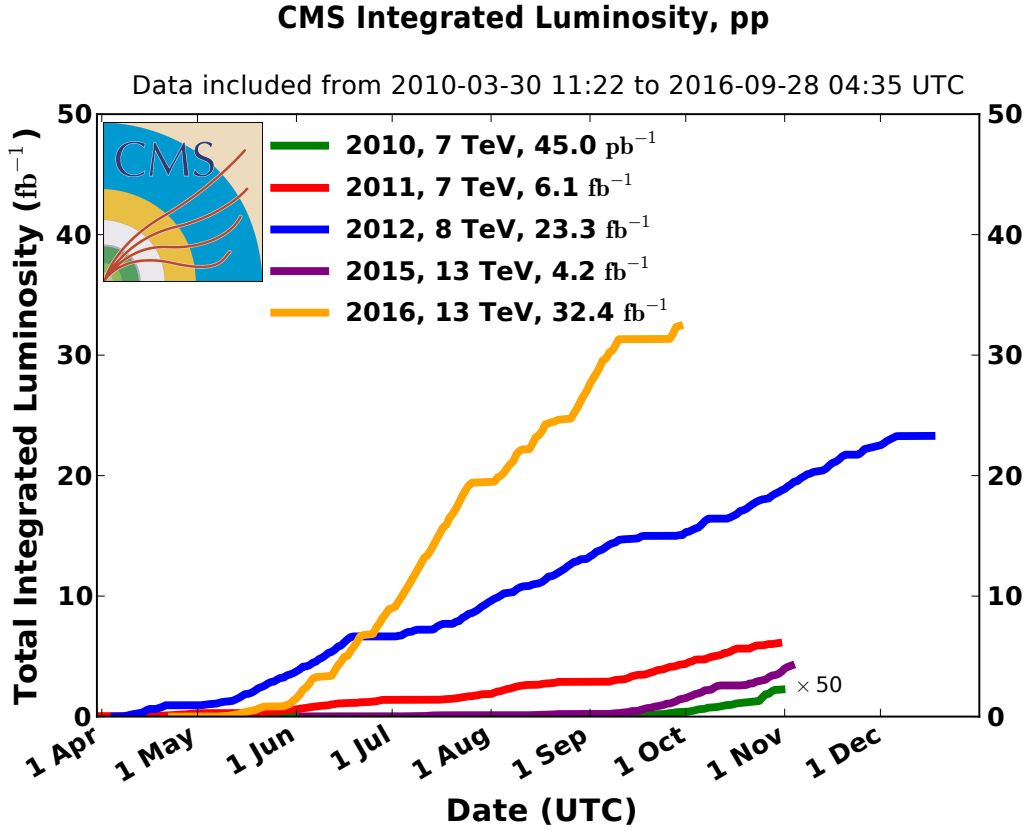


**Figure 2.2:** Overview of the integrated luminosity delivered by the LHC throughout its operation until the time of writing, as recorded by CMS. [9]

## 2.2 The Compact Muon Solenoid (CMS)

### 2.2.1 Overview

CMS is located approximately 100 m underground at access point 5 of the LHC, near the French village of Cessy. It is a layered detector over 21 m long and 14 m in diameter, weighing over 12,500 tons. It consists of a superconducting solenoid magnet 13 m long and 5.9 m in diameter, generating a 3.8 T magnetic field, which is embedded within and around the various sub-detectors, which are described in detail in this section. The layout of the CMS detector can be seen in Figure 2.3. CMS is composed of a cylindrical barrel region within and around the solenoid, and two endcaps on either side. The trackers (described in Section 2.2.2), electromagnetic calorimeter (ECAL) (described in Section 2.2.3), and hadron calorimeter (HCAL) (described in Section 2.2.4) are housed within the solenoid. Outside of the solenoid, four layers of iron act as a return yoke for the magnet and house muon detector chambers (described in Section 2.2.5). CMS

is equipped with a triggering system which is described in Section. 2.2.6. Particular attention will be given to describing the ECAL as it is the most important sub-detector in the analysis of Higgs bosons decaying to photons.

The CMS detector uses a right-handed coordinate system whereby the  $x$ -axis points towards the centre of the LHC ring, the  $y$ -axis points upwards, and the  $z$ -axis points in the direction of the counter-clockwise beam. A more convenient coordinate system is  $(\eta, \phi, z)$ , where  $\eta = -\ln[\tan(\frac{\theta}{2})]$  is the pseudorapidity (where  $\theta$  is the polar angle relative to the beam axis) and  $\phi$  is the angle relative to the  $x$ -axis in the  $(x, y)$  plane.

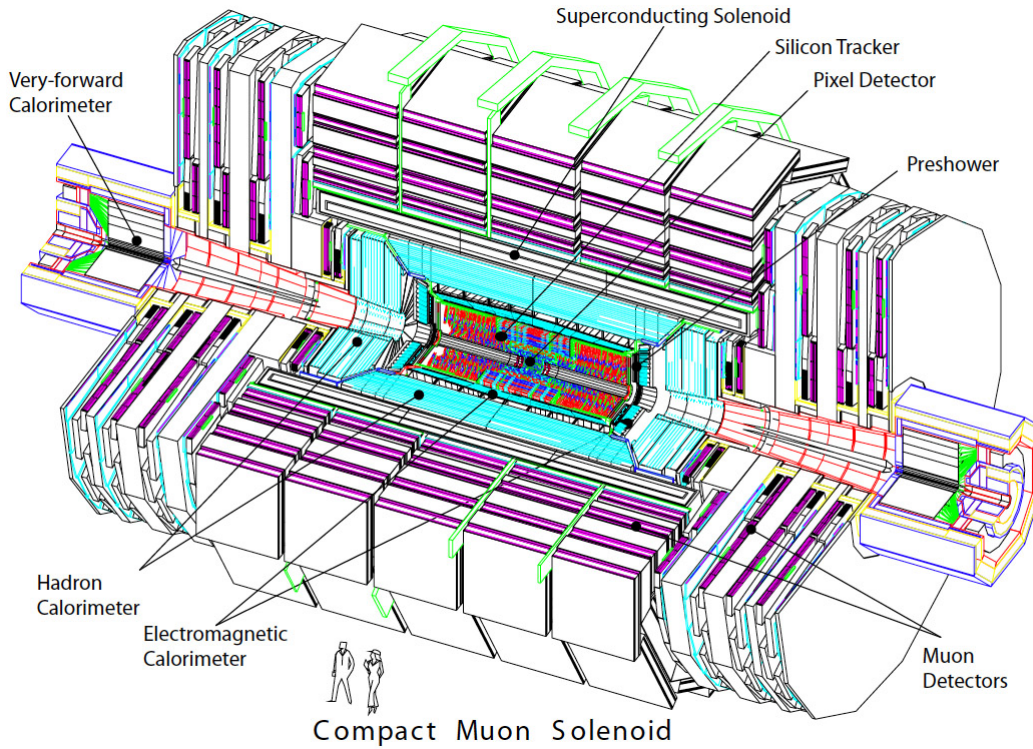


**Figure 2.3:** A cutaway diagram of the CMS detector, showing the main components and subdetectors, which are described in Section 2.2 [10].

### 2.2.2 Tracker

The closest sub-detector to the beam crossing point is the tracker [11], the layout of which can be seen in Figure 2.4. This sub-detector, which fits within a cylindrical volume 5.8 m long and 2.5 m in diameter, is used to accurately measure the momenta of charged particles which are produced during p-p collisions. The tracker consists of a barrel section (3 cylindrical layers of silicon pixel detectors close to the interaction region, surrounded

by 10 layers of silicon micro-strip detectors), and endcaps (two discs of silicon pixel detectors and 12 discs of silicon microstrip detectors). Momenta of charged particles can be measured accurately for  $|\eta| \leq 1.6$  (where particles intersect about 13 planes), and to a lesser extent for  $|\eta| < 2.5$  (where particles intersect at least 8 planes), by measuring the curvature of tracks as they bend in the strong magnetic field. The charged particles are used in particular to identify the spacial location of the interactions, or vertices, and in particular the PV. The short bunch spacing of the LHC beams as well as the large p-p cross-section mean the tracker must have a very fast response time while being resistant to radiation. This motivates the use of silicon technologies for the CMS tracker, in the form of the pixel tracker and the strip tracker.

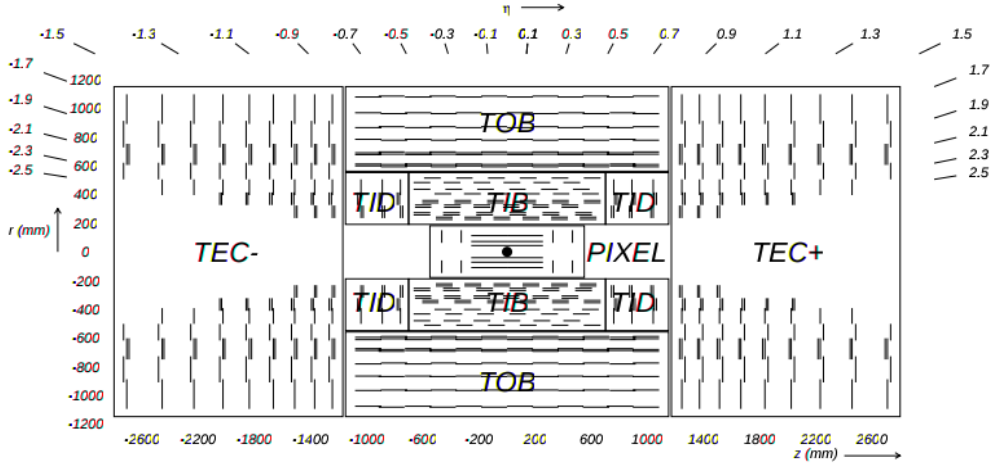


**Figure 2.4:** A diagram showing the layout of the CMS tracker components: the pixel tracker (labelled PIXEL) is the nearest to the interaction region marked by the black dot. The various sections of the strip tracker (TIB, TID, TOB, TEC+ and TEC-) are arranged around the pixel tracker. [10]

The pixel tracker is made up of 66 million  $100\,\mu\text{m} \times 150\,\mu\text{m}$  silicon pixels. As can be seen in Figure 2.4, these are arranged into three concentric cylinders in the barrel section (of radii between 4.4 cm and 10.2 cm) and two planes on each endcap. The spacial resolution of this part of the tracker is around  $10\,\mu\text{m}$  in the transverse direction. The pixel tracker also has excellent longitudinal resolution (20-40  $\mu\text{m}$ ), which is important for vertex reconstruction. [12]

The strip tracker surrounds the pixel tracker, and is composed of several sections. Four cylindrical layers form the tracker inner barrel (TIB), while the tracker inner disks (TID) are composed of three planes. Surrounding this, the tracker outer barrel (TOB) provides a further 6 cylindrical layers, while 9 planes form the tracker endcaps (TEC). The strip



tracker extends to 110 cm in radius. 9.3 million strips are used in this section of the tracker, with each strip being 10-20 cm long and  $80\text{--}183\ \mu\text{m}$  wide. The transverse spatial resolution of the strip tracker is between  $13\text{--}38\ \mu\text{m}$  in the inner section and  $18\text{--}47\ \mu\text{m}$  in the outer section. [12]

Charged particles follow helical trajectories in the CMS magnetic field, and deposit charge as they pass through the various planes and cylinders of the detector. Charge deposits in tracker modules are referred to as hits. Using multiple hits in the pixel and strip detectors, the helical trajectory can be reconstructed. The  $p_T$  of charged particles can then be extracted from the curvature of the helix. The  $p_T$  resolution is of the order of 2-3% in the  $|\eta| < 1.6$  region and up to around 11% for the outer section. Using the extrapolation from the fitted track and the longitudinal resolution of the pixel detector, tracks are grouped into common points of origin, at the PV and secondary vertices.

### 2.2.3 Electromagnetic Calorimeter (ECAL)

The ECAL [10,13] is the sub-detector whose performance is the most critical to the  $H \rightarrow \gamma\gamma$  analysis, and its layout, operation and calibration will therefore be described in more detail.

#### ECAL overview

The ECAL is made up of an array of 61,200 lead  $\text{PbWO}_4$  (lead tungstate) crystals in the barrel section and 14,648 crystals in the endcaps, arranged one crystal deep.  $\text{PbWO}_4$  was chosen because it has a short radiation length (the mean distance over which an electron loses all but  $\frac{1}{e}$  of its energy to bremsstrahlung) of 0.89 cm, and a small Molière radius (the radius of a cylinder containing on average 90% of a shower's energy) of 2.19 cm. It is also a fast scintillator and radiation resistant. These crystal properties are a central feature of the CMS detector as it allows excellent energy resolution of incoming photons.

The ECAL crystal front faces are  $22\text{ mm} \times 22\text{ mm}$  squares, corresponding to approximately  $\Delta\eta \times \Delta\phi = 0.0174 \times 0.0174$ , roughly matching the Molière radius. The individual crystal depth is approximately 26 radiation lengths, to ensure that the electromagnetic showers are fully contained within the ECAL. The array of crystals extends to  $|\eta| = 3$ , but precision measurements are only made up to  $|\eta| = 2.5$ . There are also transition regions between the ECAL barrel and endcaps around  $|\eta| = 1.5$ . The arrangement of the crystals in the ECAL can be seen in Figure 2.5.

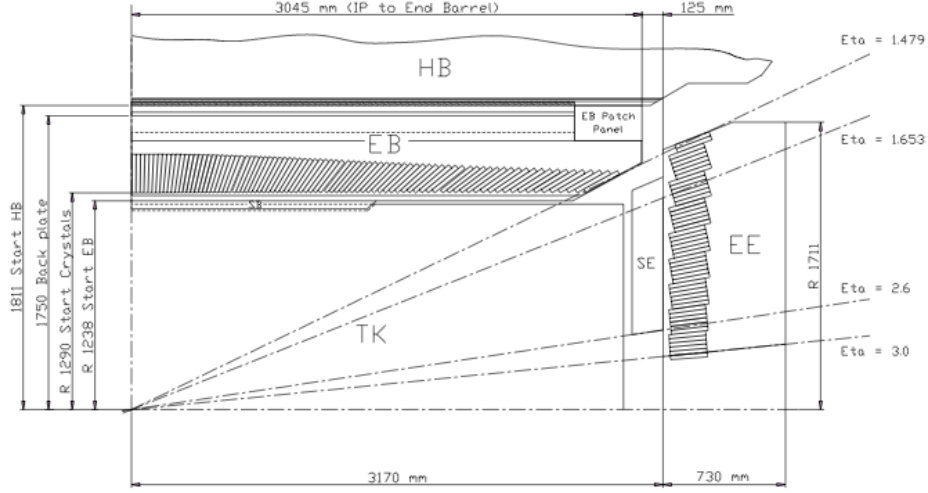


**Figure 2.5:** Schematic cross section of one quadrant of the ECAL, showing the arrangement of crystals in the ECAL barrel (EB) and endcaps (EE) [13]. The shower detector (SE, referred to as ES in the text) is also visible, as is the hadron calorimeter barrel (HB) and the tracker (TK).

Photo-diodes are attached to the back of the crystals, where the energy deposited by showers is collected. The light yield of  $\text{PbWO}_4$  is  $\sim 4000$  photoelectrons per GeV. The photo-diodes are read out by 12-bit analog to digital converters (ADC), which sample the analogue signal from the crystals at 40 MHz. Ten consecutive samples are read out and stored for each crystal, and this information is used to determine the amplitude of the pulse, and therefore the amount of energy deposited in the crystal.

The resolution of the ECAL is modelled with the following equation:

$$\left(\frac{\sigma}{E}\right)^2 = \left(\frac{S}{\sqrt{E}}\right)^2 + \left(\frac{N}{E}\right)^2 + C^2, \quad (2.3)$$

where  $S$  represents the stochastic term,  $N$  represents the noise term and  $C$  represents a constant term [10]. The design values of these parameters are approximately  $S = 2.8\% \text{ GeV}^{\frac{1}{2}}$ ,  $N = 0.12 \text{ GeV}$  and  $C = 0.3\%$ . The performance of the ECAL matched these design values during the 2012 run [14].

The ECAL is split into the ECAL barrel (EB) and the endcaps ECAL endcaps (EE), which have notably different structures and performance. The EB provides coverage in the region  $|\eta| < 1.479$ , while the EE provides coverage for  $1.556 < |\eta| < 2.5$ . The crystals in the EB are grouped into 36 supermodules, each subtending an angle of  $20^\circ$  in  $\phi$ . The crystals are arranged so that they do not point directly at the mean position of the

primary interaction vertex, but instead are positioned with a  $3^\circ$  offset in both  $\theta$  and  $\phi$ , to help improve the hermeticity of the detector. The EE is composed of two “D”-shaped sections, built up of “supercrystals” (units of 36 standard crystals). The position of the endcaps causes them to endure higher levels of radiation than the barrel region does. The EE has notably worse resolution than the EB, and this is because the calibration of the crystals is more challenging. One factor contributing to this is that the crystal transparency is affected by the high fluences in the EE. Another is that the crystal faces in units of  $\eta, \phi$  are larger in the EE than the EB, and since the energy deposited by PU is roughly constant in unit areas of  $\eta, \phi$ , the EE crystals have to deal with more noise.

The ECAL is also mounted with an additional detector, the preshower (ES), at  $1.54 < |\eta| < 2.61$ , the main purpose of which is to distinguish between  $\pi^0$  and  $\gamma$  particles. The ES is composed of two planes of lead, of 2 and 1 radiation lengths respectively, with high granularity silicon detector strips after each. The ES is used to identify  $\pi^0 \rightarrow \gamma\gamma$  photons, where both photons strike the same crystal. This is possible because the ES has a much finer granularity than the EE, so a prompt photon will register in just one strip of the ES, while a pion decaying to two photons registers in two strips. Although the EE might interpret  $\pi^0 \rightarrow \gamma\gamma$  as one highly energetic photon, the high granularity of the silicon strips in the ES allow two tracks to be identified.

## Energy measurement

The CMS ECAL crystals are designed to be approximately 1 Molière radius wide in the  $\eta$  and  $\phi$  direction, and therefore, when an electromagnetic particle hits the ECAL, the subsequent shower will spread out into adjoining crystals. In addition, photons travelling towards the ECAL can interact with the tracker material and undergo pair conversion, resulting in a wider shower. Electrons or positrons travelling towards the ECAL will be deflected in the  $\phi$ -direction by the magnetic field, and will emit photons via bremsstrahlung: in this case the radiated photons will make subsequent deposits in the ECAL. Clustering algorithms are used to recover the deposits from the main impact crystal, adjacent crystals where the energy is spread out, and other crystals which receive some of the bremsstrahlung deposits, and group them into a so-called supercluster (SC). The energy of the SC ( $E_{\text{SC}}$ ) can be expressed as

$$E_{\text{SC}} = F_{\text{SC}} \cdot (E_{\text{ES}} + G \cdot \sum_{N_{\text{crystals}}}^{i=0} (C_i \cdot S_i(t) \cdot A_i)), \quad (2.4)$$

where  $F_{\text{SC}}$  is a fine-tuned correction for imperfections in the simulation of clustering and the geometry of the detector,  $E_{\text{ES}}$  is the energy deposited in the ES,  $G$  is an ADC-to-GeV conversion factor,  $C_i$  is a factor applied to crystal  $i$  to equalise the response (also known as an intercalibration constant),  $S_i(t)$  is a time-dependent factor to correct for loss of transparency of the crystals and  $A_i$  is the amplitude of the pulse recorded in that crystal for the bunch crossing in question. [15]

## Calibration

The calibration of the ECAL involves using various techniques and physics objects to tune the values of  $S_i(t)$ ,  $C_i$  and  $G$  in Equation 2.4.

The first step is to make a time-dependent correction for loss of transparency in the crystals. Indeed, the response of ECAL crystals is worsened by exposure to radiation because of the formation of colour centres, although in shutdown periods the crystals recover some transparency through spontaneous annealing. None the less, continuous monitoring and correction of the response of the crystals is required. This is achieved using a laser which periodically (every 40 minutes during running) injects photons of wavelength 440 nm into each crystal. The degradation of the response as measured and corrected for using this mechanism is tracked in Figure 2.6. The effect of the corrections on the measured mass of the  $\pi^0$  in its decay to photons can be seen in Figure 2.7.

The next step is to determine the intrinsic crystal-by-crystal response variations, and correct these using the intercalibration constants  $C_i$ . Several methods are combined to achieve this. The first is to use the fact that the CMS ECAL is cylindrically symmetric. It is therefore expected that during a given period of time, the total energy measured by each crystal with the same value of  $\eta$  ( $\eta$ -ring) should be the same. Exploiting the  $\phi$ -symmetry of the detector, one can therefore produce an intercalibration constant for each crystal in an  $\eta$ -ring by dividing the amount of energy that was measured by that crystal in an interval of time, by the average amount measured by all crystals in that  $\eta$ -ring. Another method exploits the fact that the invariant mass of  $\pi^0$  or  $\eta$  particles (as measured in their decay to photons) should be measured the same regardless of the crystal location. Therefore, one can generate intercalibration constants by dividing the measured values of the invariant masses in each crystal by the average value measured by all crystals. Intercalibration constants produced using different methods are combined to give a final set of per-crystal corrections. It should be noted that by construction,

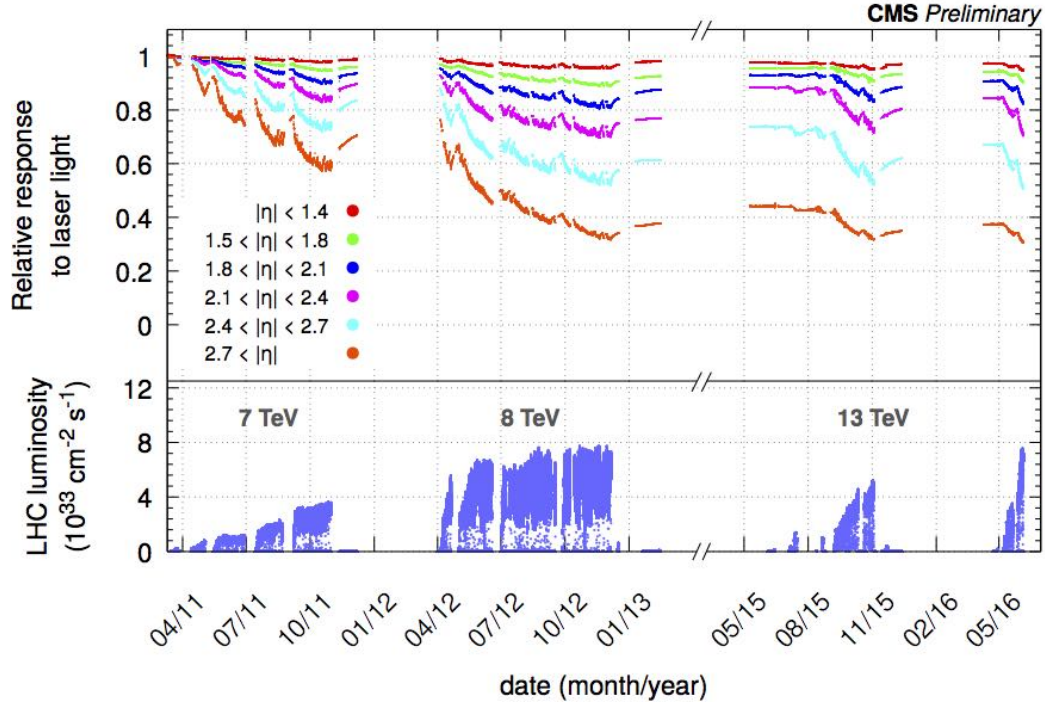


**Figure 2.6:** The response of the CMS ECAL lead tungstate crystals is shown as a function of time, and for different pseudorapidity ranges. The crystal response worsens as data are collected, due to transparency loss caused by exposure to radiation. During shutdown periods, the response recovers somewhat thanks to spontaneous annealing. [16]

the average value of the intercalibration constants is unity: these corrections leave the overall scale unchanged.

The final step in the calibration procedure is to set the global scale  $G$ , which is also the ADC-to-GeV conversion factor. This is set by comparing the measured value of the mass of the  $Z$  boson in its decay to electrons to the nominal value. Since the mass of the  $Z$  is well known and simulated, one can set the value  $G$  such that the peak of the  $Z$  invariant mass distribution coincides with the simulated value, in different bins of  $\eta$  and SC type, in order to complete the calibration.

## 2.2.4 Hadronic Calorimeter (HCAL)

The HCAL is used to identify hadrons, and measure their directions and energies. In particular, it is needed to study neutral hadrons which do not leave any hits in the tracker, or any deposits in the ECAL. Such particles need to be taken into account to accurately estimate the energies and directions of the jets produced during hadronic decays, and

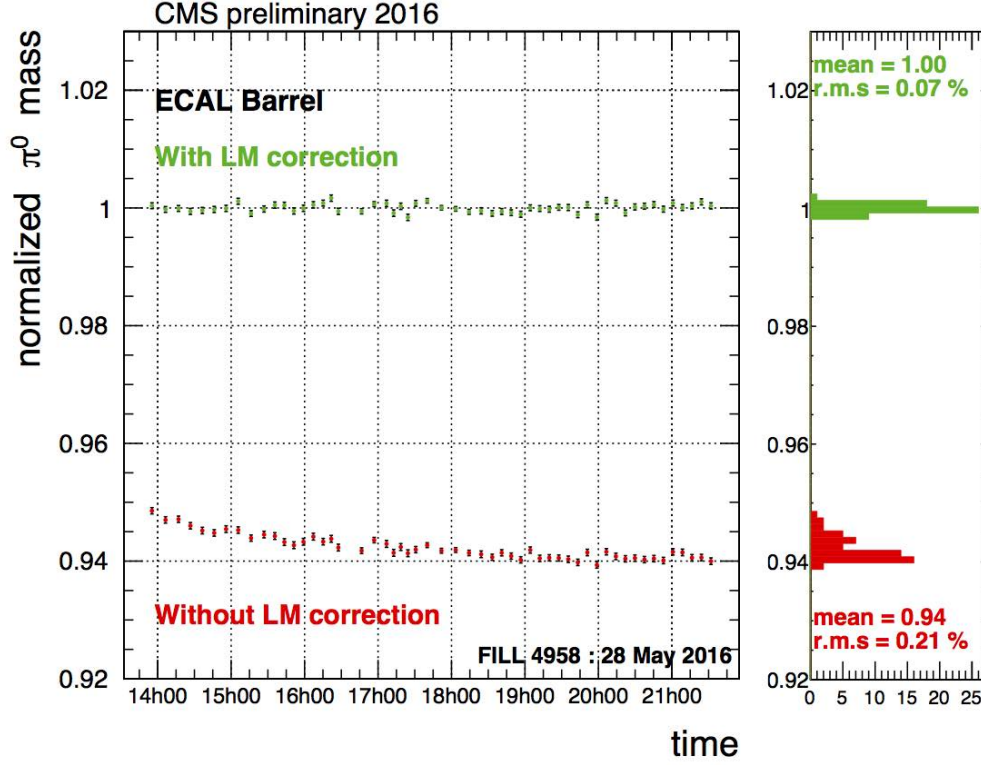


**Figure 2.7:** The normalised value of the invariant mass of the  $\pi^0$  particle in its decay to photons, as measured by the CMS ECAL barrel, with and without the Laser Monitoring (LM) corrections for crystal transparency loss, showing the degradation of the response of the lead tungstate crystals, even over a period of hours. [16]

to measure the magnitude and direction of any missing energy, which would indicate particles which did not interact by the CMS detector (e.g. neutrinos, or undiscovered weakly interacting particles).

The CMS HCAL is a sampling calorimeter, consisting of active material between absorber plates. The layout of the detector can be seen in Figure 2.8. The active material is a plastic scintillator read out by wavelength-shifting plastic fibres. The absorber plates are made of brass (or steel in the forward section). Brass is chosen as it is a non-magnetic material, and thus will not be affected by the strong magnetic field within the solenoid. The main body of the HCAL is split into the hadron calorimeter barrel (HB) with coverage up to  $|\eta| < 1.3$ , and the hadron calorimeter endcaps (HE) with coverage up to  $|\eta| < 3$ , with  $\Delta\phi \times \Delta\eta$  granularities between  $0.087 \times 0.087$  and  $0.17 \times 0.17$ . In order to accurately measure missing energy, the HCAL must be as hermetic as possible. For this reason, an additional calorimeter is appended, the forward hadron calorimeter (HF),

which gives coverage up to  $|\eta| < 5$ . This uses active quartz fibres within a steel absorber matrix. In order to fully contain hadronic showers, an additional component, the outer hadron calorimeter (HO), uses the solenoid as an absorber and is placed directly around it in the barrel region. [17]

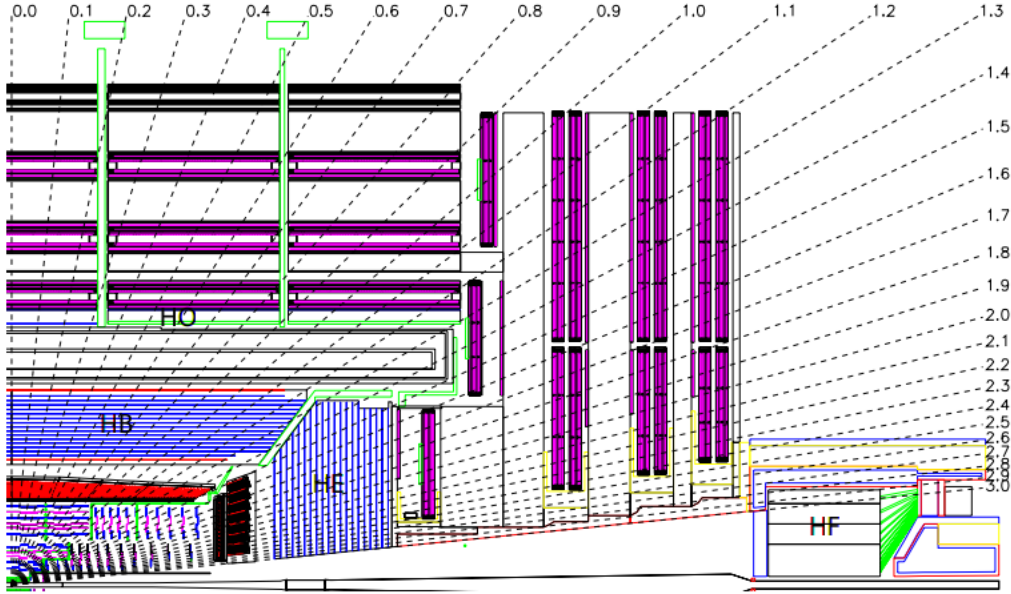


**Figure 2.8:** Schematic cross section of one quadrant of the HCAL, showing the arrangement of the various components of the sub-detector: The HB and HE surrounding the ECAL, with the HF at high  $\eta$  and the HO just outside of the solenoid. [5].

The minimum depth of the HB is 5.8 radiation lengths, rising to 11.8 when the HO is taken into account. In the endcaps, the depth is at least 10 radiation lengths [17]. The resolution of the HCAL system was measured in test beams of single pions [18] and found to be:

$$\left(\frac{\sigma}{E}\right)^2 = \left(\frac{94.3\%}{\sqrt{E}}\right)^2 + \left(\frac{8.4\%}{E}\right)^2. \quad (2.5)$$

### 2.2.5 Muon detectors

The solenoid is surrounded by the outermost sub-detector, the muon detector, which is built into and around the steel return yoke for the magnetic field. The CMS muon detection system is separated into endcap and barrel sections and is comprised of three types of detector: the drift tubes (DTs) (in the barrel), the cathode strip chambers (CSCs) (in the endcaps) and the resistive plate chambers (RPCs) (in both barrel and endcaps).

The layout of the muon detectors can be seen in Figure 2.9. All the muon detectors are gaseous detector with a similar operational principle: as charged particles travel through a chamber, the gas contained within becomes ionised and the resulting electrons drift towards the detector's anode, which gives out an electric signal.

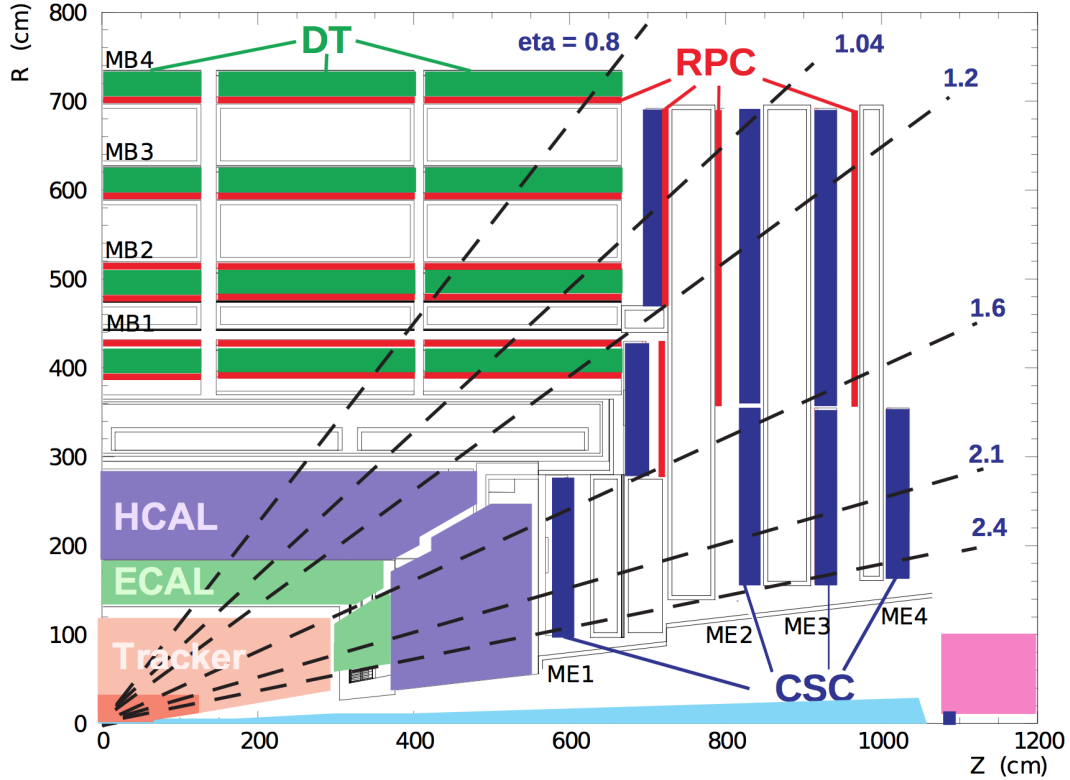


**Figure 2.9:** Schematic cross section of one quadrant of the CMS muon detector, showing the arrangement of the various components of the sub-detector: The DTs in the barrel, and CSCs in the endcaps and the RPCs in both. [19].

The barrel region has the property of a constant magnetic field and lower neutron fluences. In this section, the muon system is composed of four concentric layers of DTs, which are wire chambers filled with a mixture of gaseous Ar and CO<sub>2</sub>. Each DT station consists of twelve layers of wire chambers, with some having their wire oriented parallel to the beam axis and other perpendicular to it. This means that each DT is able to provide a position measurement in both the transverse and longitudinal planes, with 100  $\mu\text{m}$  resolution in each. The DTs are interleaved between the layers of steel return yoke, and have coverage up to  $|\eta| < 1.3$ .

In the endcaps, the field is less uniform and the neutron fluences become more important. The muon rate is also much higher than in the barrel. Therefore, a detection system



with a faster response and more resistance to radiation is needed. The CSCs, which are multi-wire chambers comprised of 6 anode wire planes interleaved among 7 cathode panels, satisfy this requirement. They are filled with a mixture of Ar, CO<sub>2</sub> and CF<sub>4</sub> gasses, and each station is also able to provide a measurement in both the longitudinal and transverse planes, with a spacial resolution around 85  $\mu\text{m}$ . There are four layers of CSCs in each endcap, installed in between the steel return yoke layers. The coverage of the CSCs is  $0.9 < |\eta| < 2.4$ .

The final detector in the muon system is the array of RPCs. These are double-gap chambers, and have a fast response with good timing resolution but worse position resolution than the DTs or CSCs. The RPCs are used as a trigger, and can also be used to resolve ambiguities in tracking when there are multiple hits in a chamber. The RPCs are installed in both the barrel and endcap sections, up to  $|\eta| < 1.6$  [5, 20]. The  $p_T$  resolution, for muons with  $p_T$  below 100 GeV, is 1-6% depending on their position within the detector. [19]

## 2.2.6 Trigger and data processing

During operation, the LHC collides bunches of protons every 25-50 ns, or equivalently the bunch crossings occur at a rate of 20-40 MHz. When the CMS detector saves the information from its sub-detector, the space taken up is of the order of 1 MB. If CMS were to save all the information from each crossing, it would therefore need to save 40 TB of data per second, which is (at the time of writing) entirely impossible to either read out or store. In addition, the vast majority of collisions are of no physics interest: many will be low-energy interactions of protons instead of head-on collisions, or will come from well-understood SM processes. Therefore, a vast reduction in the number of events selected to be saved is required, filtering out the commonplace events and saving only those which are of physics interest. This is achieved through the CMS triggering system. The trigger is used to reduce the number of events saved per second by a factor of  $10^5$ . This is achieved through two trigger levels: the level-1 trigger (L1T) and the high-level trigger (HLT).

The L1T consists of programmable, custom-designed electronics. The L1T reduces the number of output events by a factor of about 1000, allowing a maximum output rate of 30-100 kHz. As collisions occur in the CMS detector, each event is stored in a buffer, which has space for 128 bunch crossings. This gives the L1T 3.2  $\mu\text{s}$ , a very limited time, to decide whether or not to save an event. Decisions at the L1T are therefore made

based very coarse data from the different detector subsystems individually, since no time is available to exploit their full granularity and resolution, or to use detailed correlations between different sub-detectors. The short amount of time available also prohibits the use of information from the tracker, since reconstructing a path from the hits is too costly in time. Based on the coarse information available, the L1T runs a series of algorithms designed to identify events where processes of interest occur, and saves those which pass its requirements, while discarding all the others. [5].

The HLT consists of a farm of about 1000 commercially-available processors, which run basic reconstruction software and use the output to make a decision on which events to keep. The HLT provides a further reduction in the amount of data stored, reducing it by a factor of about 100, down to an output of around 400 Hz. This is achieved using simplified versions of the full CMS reconstruction software, with the full granularity of the information from the CMS sub-detectors available, including from the tracker. [5]

Events passing the HLT are then saved to disk and reconstructed using the full CMS software for use in physics analyses.



# Bibliography

- [1] L. Evans and P. Bryant, “LHC Machine”, *JINST* **3** (2008), no. 08, S08001, doi:10.1088/1748-0221/3/08/S08001.
- [2] LEP Injector Study Group, “LEP design report, volume I: The LEP injector chain; LEP design report, volume II: The LEP Main Ring”. CERN, Geneva, 1983.
- [3] M. Benedikt, P. Collier, V. Mertens et al., “LHC Design Report”. <https://cds.cern.ch/record/823808>, 2004.
- [4] ATLAS Collaboration, “The ATLAS Experiment at the CERN Large Hadron Collider”, *JINST* **3** (2008) S08003, doi:10.1088/1748-0221/3/08/S08003.
- [5] CMS Collaboration, “The CMS experiment at the CERN LHC”, *JINST* **3** (2008) S08004, doi:10.1088/1748-0221/3/08/S08004.
- [6] ALICE Collaboration, “The ALICE experiment at the CERN LHC”, *JINST* **3** (2008) S08002, doi:10.1088/1748-0221/3/08/S08002.
- [7] LHCb Collaboration, “The LHCb Detector at the LHC”, *JINST* **3** (2008) S08005, doi:10.1088/1748-0221/3/08/S08005.
- [8] C. Lefèvre, “The CERN accelerator complex. Complexe des accélérateurs du CERN.”, Dec, 2008.
- [9] CMS Collaboration, “CMS Luminosity - Public Results”. <http://twiki.cern.ch/twiki/bin/view/CMSPublic/LumiPublicResults>.
- [10] CMS Collaboration, “CMS Physics: Technical Design Report Volume 1: Detector Performance and Software”. Technical Design Report CMS. CERN, Geneva, 2006.
- [11] CMS Collaboration, “The CMS tracker system project: Technical Design Report”. Technical Design Report CMS. CERN, Geneva, 1997.

- 
- [12] CMS Collaboration, “Description and performance of track and primary-vertex reconstruction with the CMS tracker”, *JINST* **9** (2014), no. 10, P10009, doi:10.1088/1748-0221/9/10/P10009, arXiv:1405.6569.
- [13] CMS Collaboration, “The CMS electromagnetic calorimeter project: Technical Design Report”. Technical Design Report CMS. CERN, Geneva, 1997.
- [14] CMS Collaboration, “Performance of the CMS electromagnetic calorimeter and its role in the hunt for the Higgs boson in the two-photon channel”, *J.Phys.Conf.Ser.* **455** (2013) 012028, doi:10.1088/1742-6596/455/1/012028.
- [15] CMS Collaboration, “Energy Calibration and Resolution of the CMS Electromagnetic Calorimeter in  $pp$  Collisions at  $\sqrt{s} = 7$  TeV”, *JINST* **8** (2013) P09009, doi:10.1088/1748-0221/8/09/P09009, arXiv:1306.2016. [JINST8,9009(2013)].
- [16] CMS Collaboration, “CMS ECAL first results with 2016 data”. <https://twiki.cern.ch/twiki/bin/view/CMSPublic/EcalDPGResultsCMSDPS2016031>.
- [17] CMS Collaboration, “The CMS hadron calorimeter project: Technical Design Report”. Technical Design Report CMS. CERN, Geneva, 1997.
- [18] CMS Collaboration, “The CMS barrel calorimeter response to particle beams from 2-GeV/c to 350-GeV/c”, *Eur. Phys. J.* **C60** (2009) 359–373, doi:10.1140/epjc/s10052-009-0959-5, 10.1140/epjc/s10052-009-1024-0. [Erratum: *Eur. Phys. J.* C61, (2009) 353].
- [19] CMS Collaboration, “Performance of CMS muon reconstruction in  $pp$  collision events at  $\sqrt{s} = 7$  TeV”, *JINST* **7** (2012) P10002, doi:10.1088/1748-0221/7/10/P10002, arXiv:1206.4071.
- [20] CMS Collaboration, “The CMS muon project: Technical Design Report”. Technical Design Report CMS. CERN, Geneva, 1997.

# List of Acronyms

**CERN** the European Organization for Nuclear Research

**CoM** centre-of-mass

**LHC** Large Hadron Collider

**CMS** Compact Muon Solenoid

**LEP** Large Electron-Positron Collider

**PSB** Proton Synchrotron Booster

**PS** Proton Synchrotron

**SPS** Super Proton Synchrotron

**LINAC2** Linear Accelerator 2

**PU** pile-up

**SM** standard model

**ECAL** electromagnetic calorimeter

**ES** preshower

**HCAL** hadron calorimeter

**EB** ECAL barrel

**EE** ECAL endcaps

**HB** hadron calorimeter barrel

**HE** hadron calorimeter endcaps

**HF** forward hadron calorimeter

**HO** outer hadron calorimeter

**L1T** level-1 trigger

**HLT** high-level trigger

**CSCs** cathode strip chambers

**DTs** drift tubes

**RPCs** resistive plate chambers

**ADC** analog to digital converters

**SC** supercluster

**PV** primary vertex